Computational and Structural Biotechnology Journal 20 (2022) 3695–3707

COMPUTATIONAL ANDSTRUCTURAL BIOTECHNOLOGY JOURNAL

journal homepage: www.elsevier.com/locate/csbj

PP2A is activated by cytochrome *c* upon formation of a diffuse encounter complex with SET/TAF-Iβ

Miguel Á. Casado-Combreras [a], Francisco Rivero-Rodríguez [a], Carlos A. Elena-Real [a,b], Dmitry Molodenskiy [c], Antonio Díaz-Quintana [a], Marlène Martinho [d], Guillaume Gerbaud [d], Katiuska González-Arzola [a], Adrián Velázquez-Campoy [e,f,g,h], Dmitri Svergun [c], Valérie Belle [d], Miguel A. De la Rosa [a], Irene Díaz-Moreno [a,*]

[a] *Institute for Chemical Research (IIQ), Scientific Research Centre "Isla de la Cartuja" (cicCartuja), University of Seville and CSIC, Avda. Américo Vespucio, 49, 41092 Seville, Spain*
[b] *Centre de Biologie Structurale (CBS), INSERM, Centre National de la Recherche Scientifique (CNRS) and Université de Montpellier. 29 rue de Navacelles, 34090 Montpellier, France*
[c] *European Molecular Biology Laboratory, Hamburg Outstation, c/o Deutsches Elektronen-Synchrotron, Notkestr. 85, 22607 Hamburg, Germany*
[d] *Aix Marseille Univ. Centre National de la Recherche Scientifique (CNRS), BIP UMR7281, Bioénergétique et Ingénierie des protéines, 13402 Marseille, France*
[e] *Institute of Biocomputation and Physic of Complex Systems (BIFI), Joint Unit GBsC-CSIC-BIFI, Universidad de Zaragoza. C. de Mariano Esquillor Gómez, Edificio I+D, 50018 Zaragoza, Spain*
[f] *Departamento de Bioquímica y Biología Molecular y Celular, Facultad de Ciencias, Universidad de Zaragoza, C. Pedro Cerbuna, 12, 50009 Zaragoza, Spain*
[g] *Instituto de Investigación Sanitaria de Aragón (IIS Aragon), Zaragoza, Spain*
[h] *Centro de Investigación Biomédica en Red en el Área Temática de Enfermedades Hepáticas y Digestivas (CIBERehd), C. de Melchor Fernández Almagro, 3, 28029 Madrid, Spain*

ARTICLE INFO

Article history:
Received 6 April 2022
Received in revised form 4 July 2022
Accepted 4 July 2022
Available online 8 July 2022

Keywords:
Cytochrome *c*
Encounter complex
Protein phosphatase 2A
Molecular dynamics
Nuclear magnetic resonance
SET/TAF-Iβ

ABSTRACT

Intrinsic protein flexibility is of overwhelming relevance for intermolecular recognition and adaptability of highly dynamic ensemble of complexes, and the phenomenon is essential for the understanding of numerous biological processes. These conformational ensembles—encounter complexes—lack a unique organization, which prevents the determination of well-defined high resolution structures. This is the case for complexes involving the oncoprotein SET/template-activating factor-Iβ (SET/TAF-Iβ), a histone chaperone whose functions and interactions are significantly affected by its intrinsic structural plasticity. Besides its role in chromatin remodeling, SET/TAF-Iβ is an inhibitor of protein phosphatase 2A (PP2A), which is a key phosphatase counteracting transcription and signaling events controlling the activity of DNA damage response (DDR) mediators. During DDR, SET/TAF-Iβ is sequestered by cytochrome *c* (Cc) upon migration of the hemeprotein from mitochondria to the cell nucleus. Here, we report that the nuclear SET/TAF-Iβ:Cc polyconformational ensemble is able to activate PP2A. In particular, the N-end folded, globular region of SET/TAF-Iβ (a.k.a. SET/TAF-Iβ ΔC)—which exhibits an unexpected, intrinsically highly dynamic behavior—is sufficient to be recognized by Cc in a diffuse encounter manner. Cc-mediated blocking of PP2A inhibition is deciphered using an integrated structural and computational approach, combining small-angle X-ray scattering, electron paramagnetic resonance, nuclear magnetic resonance, calorimetry and molecular dynamics simulations.

Abbreviations: ANP32B, Acidic leucine-rich nuclear phosphoprotein family member B; BTFA, 3-bromo-1,1,1-trifluoroacetone; Cc, Cytochrome *c*; CD, Circular dichroism; CDK9, Cyclin-dependent kinase 9; CW, Continuous wave; D_{max}, Maximum dimension; DDR, DNA damage response; DEER, Double electron–electron resonance; DLS, Dynamic light scattering; DMEM, Dulbecco's modified Eagle's medium; DNA, Deoxyribonucleic acid; DTT, Dithiotreitol; EDTA, Ethylenediamine tetraacetic acid; EGTA, Ethyleneglycol tetraacetic acid; EPR, Electron paramagnetic resonance; FBS, Fetal bovine serum; GUI, Graphical user interface; HEK, Human embryonic kidney cells; HRP, Horseradish peroxidase; I_2PP2A, Inhibitor 2 of the protein phosphatase 2A; I_3PP2A, Inhibitor 3 of the protein phosphatase 2A; I_p/I_d, Intensity ratio of NMR resonances between paramagnetic and diamagnetic samples; INTAC, Integrator-PP2A complex; IPTG, Isopropyl-β-D-1-thiogalactopyranoside; ITC, Isothermal titration calorimetry; LB, Luria-Bertani; MD, Molecular dynamics; MTS, (1-acetoxy-2,2,5,5-tetramethyl-δ-3-pyrroline-3-methyl) methanethiosulfonate; MTSL, (1-oxyl-2,2,5,5-tetramethyl- δ −3-pyrroline-3-methyl) methanethiosulfonate; MW, Molecular weight; NAP1, Nucleosome assembly protein 1; NAPL, Nucleosome assembly protein L; NMA, Normal mode analysis; NMR, Nuclear magnetic resonance; NPT, Constant number, pressure and temperature; NVT, Constant number, volume and temperature; OD_{600}, Optical density measured at 600 nm; OPC, Optimal 3-charge, 4-point rigid water model; PCR, Polymerase chain reaction; PME, Particle mesh Ewald; PMSF, Phenylmethylsulfonyl fluoride; PP2A, Protein phosphatase 2A; PRE, Paramagnetic relaxation enhancement; PVDF, Polyvinylidene fluoride; R_g, Radius of gyration; RNA, Ribonucleic acid; RNApol II, RNA polymerase II; SAXS, Small-angle X-ray scattering; SC, Sample changer; SDSL, Site-directed spin labeling; SDS-PAGE, Sodium dodecylsulfate-polyacrylamide gel electrophoresis; SEC, Size-exclusion chromatography; SET/TAF-Iβ, SET/template-activating factor-Iβ; SET/TAF-Iβ ΔC, SET/template-activating factor-Iβ construct lacking its C-terminal domain; SPRi, Surface plasmon resonance imaging; TAF-Iα, Template-activating factor-Iα; TPBS, Tween 20-phosphate buffered saline; VPS75, Vacuolar protein sorting-associated protein 75; XRD, X-ray diffraction; WT, Wild type.

* Corresponding author.
E-mail address: idiazmoreno@us.es (I. Díaz-Moreno).

https://doi.org/10.1016/j.csbj.2022.07.009
2001-0370/

1. Introduction

The intrinsic flexibility of proteins is essential for their functionality and interactions, which are virtually key in all cellular functions. Flexible or disordered *ca.* 30-residue long segments are common in *ca.* 75% of signaling proteins [1]. Such flexibility becomes more prominent in intermolecular recognition and adaptability, strongly influencing binding affinities, thermodynamics [2] and nature of the interaction surface [3]. Dynamic recognitions involve a diffusive search along the protein surfaces, yielding an ensemble of conformations—an encounter complex—in which the two proteins diffuse along each other or participate in several collisions that properly align their binding interfaces [4]. Therefore, these processes are highly dynamic and lack a well-defined orientation [5].

When at least one of the components remains flexible upon binding, the ensemble is governed by polymorphic conformational states, keeping alternative transient contacts between specific partners [3,4]. Thus, protein intrinsic flexibility becomes prominent for intermolecular recognition and adaptability, exerting considerable influence on binding affinity or thermodynamics [2], as well as on the modulation of the binding interfaces [3]. Such a dynamic behavior is essential to fully understand the biological mechanisms relying on the molecular recognition of encounter complexes [6,7]. Therefore, it is critical to analyze their conformational ensemble, or the collection of the tridimensional structures they adopt, which remains an immense challenge in structural biology [8].

Conformational diversity makes difficult to obtain complete, well-defined structures by crystallographic methods [7,9,10]. In solution, electron paramagnetic resonance (EPR) and nuclear magnetic resonance (NMR) have widely been applied to analyze dynamic encounters [10–12]. In particular, paramagnetic relaxation enhancement (PRE)-NMR data have been used in computational complex modelling [13–15]. As well, EPR studies based on site-directed spin labeling of proteins provides rich pieces of information about their conformational behavior and the setting-up of protein interactions taking into consideration the intrinsic flexibility of protein partners [16,17]. Such consideration becomes essential in the structural study of proteins with high intrinsic dynamics, like the oncoprotein SET/template-activating factor-Iβ (SET/TAF-Iβ) whose biological functions can be strongly altered by its inherent structural plasticity.

SET/TAF-Iβ is a homodimer that functions as a histone chaperone [18,19] and modulates the DNA damage response (DDR) by retaining proteins involved in chromatin compaction and inhibition of DNA repair mechanisms around DNA breaks [20]. Recently, it has been described a role for SET/TAF-Iβ in histone H1 eviction from damaged chromatin, hence decreasing the cell survival upon DNA breaks [21]. In this context, it has been proposed that SET/TAF-Iβ facilitates the entry of DNA repair factors into the damaged sites, allowing chromatin dismantling, repair and rearrangement, as known for other nucleosome assembly protein 1 (NAP1) family members [22–23].

Besides acting as a chromatin remodeler, SET/TAF-Iβ is a well-known inhibitor of protein phosphatase 2A (PP2A), so it is also designated as the inhibitor 2 of PP2A or I_2PP2A [24,25]. Recently, PP2A has emerged as a major regulator of DDR, regulating signal transmission and controlling the action of the DNA repair mechanisms [26–28]. In recent years, PP2A has also been shown to be recruited by the Integrator RNA endonuclease complex to transcriptionally-active regions in chromatin, forming the so-called INTAC (Integrator-PP2A complex) [29,30]. Within the INTAC, PP2A is integrated as an enzyme lacking only its regulatory subunit, whose function in recruiting and handling substrates is accomplished by the Integrator subunits Ints6 and Ints8 [29]. Thenceforth, PP2A dephosphorylates the C-terminal domain of RNA polymerase II (RNApol II), which promotes transcriptional pausing and termination and, ultimately, downregulates transcription [30,31]. Actually, PP2A is considered as an important tumor suppressor protein [32] whose inactivation is commonly detected in solid tumors [33–35]. The role of PP2A in regulating INTAC-mediated transcription is essential in tumor suppression. In this context, it has recently been described the antagonistic role of INTAC and cyclin-dependent kinase 9 (CDK9), which phosphorylates the C-terminus of RNApol II and promotes the amplification of acute oncogenic transcriptional responses [36]. Indeed, mis-regulations and aberrant expressions of Integrator or some of its subunits that mediate PP2A bridging have been detected in some kinds of cancers and neurodevelopmental syndromes [29,30]. PP2A inhibition by SET/TAF-Iβ plays indeed a relevant role in tumor progression and DDR control. In this context, SET/TAF-Iβ is upregulated in a variety of tumors [37,38]. Additionally, PP2A downregulation by SET/TAF-Iβ has been proposed as the main cause of tau protein hyperphosphorylation and subsequently, Alzheimer's disease progression [39–41].

Major SET/TAF-Iβ functions, such as histone chaperone and PP2A inhibition activities, mainly rests on its globular "earmuff" domains [18,42,43]. The chaperone is a homodimer, each monomer comprising an N-terminal dimerization helix, followed by the so-called earmuff domain and an acidic disordered stretch at the C-end [18] (Fig. 1A). SET/TAF-Iβ orthologues—such as yeast NAP1 [44] and vacuolar protein sorting-associated protein 75 (VPS75) [45], and *Plasmodium falciparum* nucleosome assembly protein L (NAPL) [46]—share the structural architecture of SET/TAF-Iβ and bind histones through the groove between their globular domains, which are negatively charged and contain flexible, unstructured segments. Interestingly, the hydrophobic evolutionary conserved segments connecting the dimerization helices with the earmuffs are responsible for the aperture of the groove, which is crucial for the binding of histone dimers [45]. Remarkably, such groove substantially narrows in the crystallographic structure of SET/TAF-Iβ ΔC, a construct lacking its C-terminal acidic unstructured stretches (residues 226–277; Fig. 1A), when compared to those of NAP1 and VPS75 [18,45]. It suggests that SET/TAF-Iβ conformational dynamics changes the relative orientation of the earmuffs so as to accommodate histones or other partners of the chaperone [47].

Recently, we reported that SET/TAF-Iβ is targeted by cytochrome *c* (C*c*) upon migration of the hemeprotein from mitochondria to the cell nucleus under DNA damage conditions, leading to the impairing of the nucleosome assembly activity of the chaperone [47,48]. Besides, it has been shown that nuclear C*c* also binds to the histone chaperone acidic leucine-rich nuclear phosphoprotein 32 family member B (ANP32B), also named as inhibitor 3 of PP2A (I_3PP2A) [49].

In this work we demonstrate how C*c* blocks the SET/TAF-Iβ-mediated inhibition of PP2A. We also show that PP2A inhibition and C*c* binding abilities of SET/TAF-Iβ pivot over the globular portion of the oncoprotein, comprised within SET/TAF-Iβ ΔC. To deeply understand the diffuse events that govern the recognition between SET/TAF-Iβ ΔC and C*c,* we resorted to a methodological formula that primarily considers the flexibility and dynamics exhibited by the chaperone and its transient contacts with C*c*. Accordingly, we here report a biophysical integrative approach, including a flexible model of SET/TAF-Iβ ΔC. Actually, our molecular dynamics (MD) simulations and small-angle X-ray scattering (SAXS) analysis evidence the highly dynamic nature of SET/TAF-Iβ ΔC and provide a structural model in solution. SAXS, PRE-NMR, site-directed spin labeling (SDSL)-EPR and ^{19}F NMR analyses allowed us to fully characterize the abovementioned encounter complex, showing how C*c* preferably samples the earmuff domains

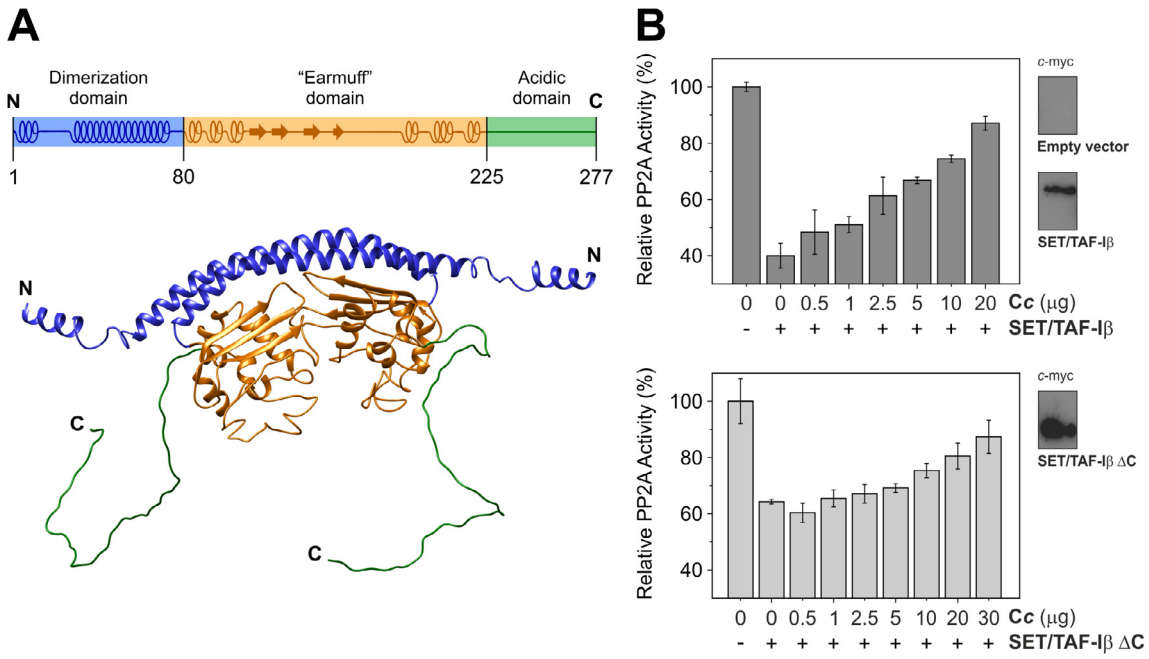

Fig. 1. Cytochrome *c* blocks PP2A inhibition mediated by SET/TAF-Iβ and SET/TAF-Iβ ΔC. (A) Domain organization and ribbon representation of the structural model of SET/TAF-Iβ. Dimerization domain (residues 1–80) is represented in blue, the earmuff domain (81–225) in gold, and the unstructured acidic domain (226–277) in green. The structural model was built using MODELLER [66] to trace the earmuff loops and C-terminal acidic domains, which were not visible in the crystallographic structure (PDB entry 2E50 [16]). (B) Relative PP2A activity of extracts from HEK293T cells transfected with empty pCDNA3.1 vector (-), pCDNA3.1-SET/TAF-Iβ (+) (*Upper*) or pCDNA3.1-SET/TAF-Iβ ΔC (+) (*Lower*), upon addition of increasing amounts of recombinant Cc. Data shown are the mean ± SD of three independent experiments. Western-blots of cell extracts against *c*-myc tag checking transfection with both SET/TAF-Iβ species are shown in each panel. (For interpretation of the references to colour in this figure legend, the reader is referred to the web version of this article.)

at SET/TAF-Iβ ΔC forming a dynamic ensemble of multiple conformations. Overall, this work evinces the molecular basis for a new regulatory function for extra-mitochondrial Cc based on hindering the SET/TAF-Iβ-mediated PP2A inhibition, making thus use of an integrative conception of structural determination methods.

2. Materials and methods

2.1. DNA constructs

The SET/TAF-Iβ and SET/TAF-Iβ ΔC genes were cloned into the pcDNA3.1 vector [39] for their expression in mammalian cells to perform PP2A inhibition assays. The *c*-myc tag was included at the C-terminus of each construct to be detectable by Western-blot.

Recombinant expression of SET/TAF-Iβ species was achieved by cloning SET/TAF-Iβ ΔC (residues 1-225), containing an N-terminal 6xHis tag, into the pET14b vector under the T7 promoter [50]. To graft both nytroxide and fluorine tags into the earmuff domains or the α-helices responsible for protein dimerization, Cys residues were introduced at different positions of SET/TAF-Iβ ΔC. Site-directed mutagenesis was performed by polymerase chain reaction (PCR), using the pET14b-SET/TAF-Iβ ΔC construct. The following primers were designed:

5′- CCAACCATTTTTTTGCAAGAGGTCAGAA -3′ and.
5′- TTCTGACCTCTTGCAAAAAAATGGTTGG -3′ for Q69C;
5′- CCATCCACAAGTGTGTGCACTGCTTGG -3′ and.
5′- CCAAGCAGTGCACACACTTGTGGATGG -3′ for S93C;
5́- GCAGAATAAAGCCTGCAGGAAGAGGCAG -3′ and.
5′- CTGCCTCTTCCTGCAGGCTTTATTCTGC -3′ for S178C;
5′- CTGATGCAGGTTGTGATGAGTTAGGAG -3′ and.
5′- CTCCTAACTCATCACAACCTGCATCAG -3′ for A201C;
5′- GTTCCCGATATGTGCTAAGGATCCG -3′ and,
5′- CGGATCCTTAGCACATATCGGGAAC -3′ for D226C.

It is worth to be mentioned that mutant D226C includes a Cys insertion at the C-end of SET/TAF-Iβ ΔC, since this construct comprises residues 1 to 225.

The DNA encoding for Cc was already cloned into the pBTR1 expression vector, along with yeast heme lyase for the proper heme group assembly [51,52].

2.2. Cell cultures

Human embryonic kidney 293 T (HEK293T) cells were cultured in Dulbecco's modified Eagle's medium (DMEM, *Sigma Aldrich*) supplemented with 10% heat-inactivated fetal bovine serum (FBS), 2 mM L-glutamine, 100 U/mL penicillin, 100 μg/mL streptomycin, and maintained at 37 °C in a humidified 5% CO_2 atmosphere.

2.3. PP2A inhibition assays

To perform PP2A inhibition assays, 2.5 × 10^6 HEK293T cells were cultured in 150 mm diameter plates approximately 70% confluence was reached. Cell transfection with both SET/TAF-Iβ, SET/TAF-Iβ ΔC or the empty vector was performed with calcium phosphate as previously described [53]. 48 h after transfection, cells were harvested in lysis buffer, containing 10 mM Tris-HCl (pH 7.4), 50 mM NaCl, 1 mM ethyleneglycol tetraacetic acid (EGTA) and 1 mM ethylenediamine tetraacetic acid (EDTA), and sonicated (10 s, 10% amplitude) on ice. Cell debris were removed by centrifugation at 16,300 × g during 15 min. Protein expression was confirmed by Western-blot detection.

Western-blot assays were performed by separating proteins in a sodium dodecyl sulphate–polyacrylamide gel electrophoresis (SDS-PAGE, 12% acrylamide) and transferring them onto polyvinylidene fluoride (PVDF) membranes using a *BioRad* Mini

Trans-Blot transfer cell. Next, membranes were blocked with 5% non-fat dry milk in phosphate buffered saline (PBS) containing 0.1% Tween 20 (TPBS) for 1 h. Immunodetection was performed using an antibody against *c*-myc tag, clone 4A6 (catalog number 05–724, *EMD Millipore*) and a secondary horseradish peroxidase (HRP)-conjugated mouse IgG (catalog number A9044, *Sigma Aldrich*).

Relative PP2A activity was measured as previously described [39] with minor modifications. Briefly, cell extracts (120 μg of protein, determined by Bradford method [54]) were incubated with increasing concentrations of recombinant C*c* in the reaction buffer, containing 50 mM Tris-HCl (pH 7.4), 0.1 mM $CaCl_2$ and 2.5 mM $NiCl_2$, as well as 1 mg/mL *p*-nitrophenyl phosphate as enzyme substrate. Reactions were stopped with 13% K_2HPO_4. PP2A activity was followed by measuring absorbance values at 410 nm, using a plate reader spectrophotometer (model 680, *BioRad*). For each assay, data were normalized to extracts transfected with the empty vector. Each experimental data was the mean ± SD value of at least three independent measurements.

2.4. Protein expression and purification

SET/TAF-Iβ ΔC wild type (WT) construct and its Cys mutants were expressed in *E. coli* BL21 (DE3) strain. Firstly, Luria-Bertani (LB) pre-cultures, supplemented with ampicillin (100 μg/mL), were grown at 37 °C up to saturation. Afterwards, they were used to inoculate the final cultures, which were grown at 37 °C until an optical density measured at 600 nm (OD_{600}) of 0.6–0.8 was reached. 1 mM isopropyl-β-D-1-thiogalactopyranoside (IPTG) was then added to induce protein expression during 24 h at 30 °C. Cells were collected by centrifugation at 3,500 × g for 10 min (4 °C) and then, resuspended in 20 mM Tris-HCl buffer (pH 8.0), 800 mM NaCl, 10 mM imidazole. Cell suspension was incubated during 15 min at room temperature with 0.01% phenylmethylsulfonyl fluoride (PMSF), 0.2 mg/mL lysozyme, 0.02 mg/mL DNase I and 1x protease inhibitors (cOmplete Mini, EDTA-free; *Roche*) before sonication (4 min, 35% amplitude). Insoluble debris was removed by centrifugation at 48,000 × g for 40 min (4 °C). SET/TAF-Iβ ΔC species were purified from the protein extract by affinity chromatography, using a Ni Sepharose 6 Fast Flow (*GE Healthcare*) column. For Cys mutants, a concentration of 5 mM of dithiotreitol (DTT) was kept during purification. Protein purity was verified by SDS-PAGE (Fig. S1) and their aggregation state by dynamic light scattering (DLS) (Fig. S2). Pure SET/TAF-Iβ ΔC samples were monodisperse according to DLS analyses, yet displaying a slightly high polydispersion index (0.303 ± 0.023). The smooth shapes of the autocorrelation functions (*ca.* 0.75 amplitude and flat baseline; Fig. S2, inset) indicates this is due to molecular flexibility rather than denaturation or aggregation. Protein concentrations were assessed by Bradford method [54].

C*c* was expressed in the *E. coli* BL21(DE3) strain, as previously described [52]. First, a 50 mL LB preculture, supplemented with ampicillin (100 μg/mL), was grown at 37 °C up to saturation. Then, 5 mL were used to inoculate 2.5 L LB cultures in 5 L Erlenmeyer flasks. These cultures were incubated during 24 h at 30 °C under agitation. Afterwards, cells were harvested and resuspended in 10 mM Tricine-NaOH (pH 8.5). Cell suspension was treated with 0.01% PMSF, 0.2 mg/mL lysozyme and 0.02 mg/mL DNase I and next, cells were sonicated for 3 min at 30% amplitude and centrifuged 40 min at 48,000 × g (4 °C) to remove the cellular debris. For NMR experiments, ^{15}N-labeled C*c* was expressed in minimal media (M9), supplemented with $^{15}NH_4Cl$ as a nitrogen source, by following a similar procedure. Protein purification was based on cation exchange chromatography using a *Foresigth Nuvia S* 5 mL column (*BioRad*). The purity and homogeneity of C*c* preparations were confirmed by SDS-PAGE. C*c* concentration was followed by UV–Vis spectrophotometry, using an extinction coefficient at 550 nm of 28.92 mM^{-1} cm^{-1}.

Finally, proteins were concentrated using 3 or 10 kDa cut-off *Merck Millipore* concentrators and dialyzed against the appropriate buffer.

2.5. Dynamic light scattering

DLS measurements were carried out to determine the oligomerization state of the SET/TAF-Iβ ΔC samples. Samples were prepared at 0.8 mg/mL in 10 mM sodium phosphate (pH 7.4). DLS experiments were performed at 25 °C in a Zetasizer Nano ZS (*Malvern Instruments*).

2.6. Circular dichroism

Circular dichroism (CD) spectra were recorded at 20 °C in the far UV region (190–250 nm) at 0.2 nm/min, using a 1-mm thick quartz cuvette on a J-815CD Spectropolarimeter (*Jasco*), equipped with a Peltier temperature control system. All the measurements were taken for 0.1 mg/mL for the different SET/TAF-Iβ ΔC Cys mutants, in 10 mM sodium phosphate (pH 6.3) in D_2O. Three scans were averaged for each sample. Mean ellipticity values per residue ($[\theta]_{mrw,\lambda}$) were calculated as described by Kelly *et al.* [55].

2.7. Spin and ^{19}F labeling

SET/TAF-Iβ ΔC Cys mutant samples were dialyzed in 20 mM sodium phosphate (pH 7.4) and 50 mM NaCl, containing 1 mM of DTT. Then, DTT was removed by gel filtration using a desalting PD-10 column (*GE Healthcare*). Immediately, fluorine label BTFA (3-bromo-1,1,1-trifluoroacetone), paramagnetic spin label MTSL ([1-oxyl-2,2,5,5-tetramethyl-δ3-pyrroline-3-methyl] methanethiosulfonate; *Toronto Research Chemicals Inc.*, Toronto, Canada) or diamagnetic label MTS ([1-acetoxy-2,2,5,5-tetramethyl-δ-3-pyrroline-3-methyl] methanethiosulfonate; *Toronto Research Chemicals Inc.*, Toronto, Canada) were added to the sample at a 7 to 10-fold molar excess from concentrated stock solutions in acetonitrile. The labeling reaction was carried out at 4 °C, in the dark, under gentle stirring and continuous flow of Ar during 1 h for spin labeling, whereas overnight for ^{19}F labeling. Excess of unbound label was removed using a desalting column (PD-10) in the elution buffer (10 mM sodium phosphate, pH 6.3) that was prepared in D_2O for EPR experiments. The fractions containing the labeled variants were pooled and concentrated by ultrafiltration using 30 kDa cut-off *Merck Millipore* concentrators. The secondary structure of SET/TAF-Iβ ΔC Cys mutants was assessed before and after spin labeling, as well as its stability, by CD (Fig. S3). For double electron–electron resonance (DEER) experiments, final protein concentrations of 80 μM were used and 30% (v/v) deuterated glycerol-d8 was added just before a rapid freezing in liquid N_2 to prevent excluded volume effects and heterogeneous protein concentration.

2.8. Isothermal titration calorimetry

Isothermal titration calorimetry (ITC) experiments were performed in a Nano ITC Low Volume (*TA Instruments*, USA) at 25 °C. The experiments consisted of 17 injections of 300 μM reduced C*c*, 2.91 μL each, in 10 mM sodium phosphate (pH 7.4) into the sample cell, initially filled with 30 μM solution SET/TAF-Iβ ΔC. The same experiment was performed in the presence of 100 mM KCl. Injection interval was set to 180 s, allowing the return of the thermal power signal to the baseline before the next injection. During the titration, stirring was constantly maintained at 300 rpm. The reference cell was filled with ultra-pure water and all samples

were degassed prior to the experiments. Injection heats normalized per mole of injectant *vs.* molar ratio data were fitted to an independent binding site model.

2.9. Surface plasmon resonance

Surface plasmon resonance imaging (SPRi) experiments were carried out using a SPRi-Plex II (*Horiba*) equipment. SET/TAF-Iβ ΔC species at different concentrations (5 and 10 μM) were covalently coupled to a CO-chemistry biochip surface. Bovine serum albumin (BSA) was coupled at reference spots as a control. C*c* solutions at 500 nM, 2.5 μM and 5 μM were passed, at least three times each, onto the biochip surface at a 50 μL/min flow rate. Measurements were performed at 25 °C, using 10 mM sodium phosphate (pH 6.3) as running buffer. Data processing and analysis was performed using Origin 2016 (*OriginLab Corporation*). SPR response curves were obtained as average of the three independent injections and simultaneously fitted to a one-site binding model.

2.10. Small-angle X-ray scattering

SAXS data on SET/TAF-Iβ ΔC and SET/TAF-Iβ ΔC:C*c* complex were collected at the P12 beamline [56] of the European Molecular Biology Laboratory at the PETRA III storage ring (DESY, Hamburg, Germany). Preparatory SET/TAF-Iβ ΔC dilution series were measured to evaluate possible interparticle interactions and to select SET/TAF-Iβ ΔC working concentrations. For SET/TAF-Iβ ΔC titration with C*c*, both size-exclusion chromatography (SEC)-coupled SAXS (SEC-SAXS) [57] and sample changer (SC) [58] were used. Measurements in SC mode were carried out using a fixed concentration for SET/TAF-Iβ ΔC of 6.1 mg/mL at different titration levels of C*c*, ranging from 1:0 to 1:4 molar ratios. In the SC mode, samples and buffer underwent a continuous flow during SAXS measurements at 20 °C, consisting of 40 × 100 ms exposures, for a total exposure time of 4 s. The data were recorded on a Pilatus 6M detector at the wavelength λ = 1.24 Å, covering the momentum transfer range $0.03 < s < 7.3$ nm^{-1} ($s = 4\pi \sin\theta/\lambda$, 2θ being the scattering angle).

The experimental data were processed using standard procedures [59]. Radius of gyration (R_g) and particle distance distribution function [$P(r)$] were calculated with Autorg and Datgnom [60], respectively. SET/TAF-Iβ ΔC molecular weight (MW) was assessed by the absolute calibration method [61] and also by the concentration-independent approaches and its credibility intervals were determined by means of Bayesian statistics [62]. The scattering from the atomistic models were computed, fitted to the experimental data by CRYSOL [63] and the models were further refined using normal mode analysis (NMA) in SREFLEX [64].

The arrangement of SET/TAF-Iβ ΔC monomers and C*c* molecules into the complex was analyzed by rigid body modelling using CORAL [65]. No symmetry restrictions were imposed.

Raw experimental data, models, and fits were deposited to the SASBDB data bank with the following accession codes: SASDN77 and SASDN87.

2.11. Molecular dynamics computations

MD computations on SET/TAF-Iβ ΔC were carried out using the AMBER 16 package [66] and the AMBER-14SB force field libraries [67]. The loop-refined model of SET/TAF-Iβ ΔC—based on X-ray diffraction (XRD) analysis (PDB entry 2E50 [18])—were the initial coordinates. N-terminal helices and missing loops in the XRD structure were modelled by simulated annealing using MODELLER [68]. The topology and coordinate files needed for MD calculations were generated by using the LEAP module of the AMBER 16 package [66]. Simulations were performed under periodic boundary conditions, using an orthorhombic cell geometry and particle mesh Ewald (PME) electrostatics with an Ewald summation cut off of 8 Å. The system was neutralized with sodium counter-ions according with the total charge of the protein and solvated using an optimal 3-charge, 4-point rigid water model (OPC) molecules [69]. After 500 steps of energy minimization of protein sidechains, solvent and counter-ions were subjected to 500 steps of steepest descent minimization followed by 500 ps isothermal and isobaric (NPT)-MD computations. Isotropic molecule position scaling and a pressure relaxation time of 2 ps at 25 °C were used. Temperature was regulated using a Langevin integrator [70] with a collision frequency of 5 ps^{-1}. When the system density reached a *plateau*, an energy-minimization was performed previously to isothermal and isochoric (NVT)-MD computations at 25 °C for 23 ns. The SHAKE algorithm [71] was used to constrain bonds involving hydrogen atoms. Average energies of this run were used to simulate a 200 ns evolution by accelerated-MD computations [72]. MD simulations on full-length SET/TAF-Iβ were carried out with the OpenMM software [73] using a Langevin integrator with a friction coefficient of 1 ps^{-1}. For each system, evolution times of 100 ns were simulated at 298 K and 1 atm, with 5,000 previous energy minimization steps of 2 fs. The PTRAJ module of AMBER [74] was used for trajectory analysis.

Every snapshot from SET/TAF-Iβ ΔC trajectories was analyzed with the CRYSOL program of ATSAS package [63,75] to check compatibility with the SAXS data. Contact maps of full-length SET/TAF-Iβ were created with the Contact Map Explorer tool of the MDTraj library [76]. Intramolecular contacts were accounted when the distance between any atom of the considered residues was less than 4.5 Å. Molecular graphics were performed with Chimera [77].

2.12. Electron paramagnetic resonance

Continuous-wave (CW)- and pulsed-EPR experiments (DEER) were carried out on MTSL spin-labeled SET/TAF-Iβ ΔC single-Cys mutants, in both the absence and the presence of reduced C*c* in a 1:2 SET/TAF-Iβ ΔC:C*c* molar ratio.

X-band continuous-wave room temperature experiment (23 °C) EPR spectra were recorded on an ELEXSYS E500 *Bruker* spectrometer, equipped with a Super High Q Sensitivity resonator operating at X-band (9.9 GHz). The microwave power was 10 mW, the magnetic field modulation amplitude 0.1 mT and the frequency modulation 100 kHz. Spin concentration was obtained by measuring the double integral of EPR signals, compared to a reference sample. For all variants, high spin-labeling yields—ranging from 80 to 100%—were obtained.

DEER experiments were performed on a *Bruker* ELEXSYS E580 at Q-band (34 GHz), using an EN 5107D2 resonator. The system was equipped with an Oxford helium cryostat temperature regulation unit. Data acquisition was performed at -213 °C. This temperature was optimized according to relaxation times (spin–lattice relaxation time T_1 and phase memory time T_m), measured at variable temperatures in order to maximize T_m for optimal echo detection and minimize T_1 for optimal repetition time. Four-pulse DEER experiments were run with pulse durations of 20 ns (π/2) and 40 ns (π), interpulse delays τ_1 of 200 ns and τ_2 adjusted according to T_m. The pump frequency was centered at the maximum resonance while the observer frequency was 56 MHz lower. Undesirable echoes were suppressed using an 8-step phase cycling. Total acquisition time was between 8 and 12 h. Inter-label distance distributions were calculated using DeerAnalysis 2018 software [78]. The dipolar evolution datasets after background correction were processed with Tikhonov regularization. The regularization factor *a* was chosen according to the L-curve criterion, based on a compromise between smoothness and resolution.

2.13. ^{19}F and paramagnetic relaxation enhancement nuclear magnetic resonance

1D ^{19}F NMR measurements of BTFA-labeled SET/TAF-Iβ ΔC species upon the addition of reduced C*c* or BSA, both in a 1:2 M ratio, were performed on a *Bruker* Avance 600 MHz at 25 °C. These experiments were carried out in 10 mM sodium phosphate buffer (pH 6.3), with 10% D_2O to adjust the lock signal.

PRE-NMR measurements were performed on samples containing 92 μM of ^{15}N-labeled C*c* and 23 μM of each SET/TAF-Iβ ΔC single-Cys mutant conjugated with MTS or MTSL probes, forming a 1:0.25 complex. Samples were prepared in 10 mM sodium phosphate (pH 6.3) containing 10% D_2O. Samples were maintained in Ar atmosphere, in order to minimize ^{15}N-C*c* oxidation. All measurements were performed on a *Bruker* Avance III 500 MHz, equipped with a 5 mm TCI cryoprobe, at 25 °C. Spectra were acquired and processed by TopSpin NMR software (*Bruker*) and analyzed by NMRFAM-SPARKY [79]. The assignments for C*c* ^{1}H-^{15}N resonances were available (BMRB entry 25907 [80]).

For each observed amide proton, the intensity ratio of ^{1}H-^{15}N resonances for C*c* in complex with either paramagnetic (MTSL) or diamagnetic (MTS) variants of SET/TAF-Iβ ΔC mutants (I_p/I_d) was calculated. Obtained I_p/I_d ratios were divided by the mean of the ten higher I_p/I_d values for each complex to get normalized I_p/I_d.

3. Results

3.1. Cytochrome c blocks SET/TAF-Iβ-mediated inhibition of PP2A

PP2A inhibition by SET/TAF-Iβ mainly rests on the chaperone earmuff domains, which are actually responsible for their histone chaperoning [18,42,43]. Such domains likewise settle the SET/TAF-Iβ interaction with C*c* upon nuclear translocation of the hemeprotein following DNA breaks, thereby altering the nucleosome remodeler activity of SET/TAF-Iβ [47,48]. Under that cellular stress, C*c* also binds to another histone chaperone, namely ANP32B, regulating the PP2A inhibitory function of the latter [49]. These facts led us to hypothesize that the hemeprotein could play a similar role controlling PP2A activity through SET/TAF-Iβ inhibition.

To prove this hypothesis, PP2A activity was measured in HEK293T cell extracts overexpressing full-length SET/TAF-Iβ or the construct that exclusively contains dimerization and earmuff domains (SET/TAF-Iβ ΔC) (Fig. 1A). Upon addition of increasing amounts of recombinant C*c*, the PP2A activity levels dropped to *ca.* 40% or 65% in the presence of SET/TAF-Iβ or SET/TAF-Iβ ΔC, respectively, over control cells transfected with empty vector (Fig. 1B). This suggests that SET/TAF-Iβ ΔC is still capable of inhibiting PP2A activity, albeit to a lesser extent as compared with full-length SET/TAF-Iβ. Although the SET/TAF-Iβ earmuffs were described as the main domains responsible for their PP2A inhibition activity [39,42,43], our results reveal that the C-terminal domains strengthen the PP2A inhibition by an indirect, unexplored mechanism.

Adding C*c* resulted in a concentration-dependent recovery of PP2A activity of extracts containing full-length SET/TAF-Iβ (Fig. 1B, *upper*). As expected, this effect of the C*c* concentration over the recovery of the PP2A activity was less pronounced when expressing SET/TAF-Iβ ΔC (Fig. 1B, *lower*). In fact, an additional titration point (30 μg of C*c*) was needed in this case to reach a similar recovery level than the obtained under full-length SET/TAF-Iβ inhibition conditions. Nevertheless, C*c* alleviates the PP2A inhibition exerted by SET/TAF-Iβ even when the C-terminal acidic stretches of the histone chaperone were removed. Faster restoration of PP2A activity detected when using full-length SET/TAF-Iβ (Fig. 1B, *upper*) could stem from additional contacts of the hemeprotein with the acidic C-terminal domains of the chaperone, as previously observed [43]. Altogether, these results points to a competition between C*c* and PP2A for binding SET/TAF-Iβ earmuff domains.

3.2. SET/TAF-Iβ ΔC is a flexible protein

To understand the molecular basis of SET/TAF-Iβ ΔC inhibition by C*c*, we firstly assessed the dynamic behavior of such construct. In the available XRD model, SET/TAF-Iβ ΔC forms a dimer with a headphone-like shape (PDB code 2E50 [18]) in which several stretches are missing (145–152, 167–188 and 195–200) in both monomers. These absent stretches correspond to mobile regions and hence, we analyzed their dynamics. To this end, we employed a preliminary loop-refined model which contained these loops, based on the XRD coordinates [47]. Then, a 200 ns trajectory of the homodimer was computed (Fig. S4). Despite its high content in secondary structure, the whole molecule exhibited highly mobility (Fig. S4A), displaying stretching and twisting distortions along the trajectories besides the expected fluctuations of the above-mentioned loops (Fig. S4B). The dimerization domain acted as a hinge, enabling rigid-body motions, changing the relative orientation between the two globular domains.

Considering the high flexibility exhibited by SET/TAF-Iβ ΔC, we performed SAXS on this construct to clarify whether the structure of SET/TAF-Iβ ΔC in solution differs from the XRD model. Fig. 2A-B (*left* panels) displays the fits of the scattering intensity profile using CRYSOL [63]. When the initial, loop refined XRD coordinates were used, their fit to the SAXS experimental profile was significantly worse (χ^2 = 8.29, Fig. 2A, *left*) than the fit by the structure closest to the average from the MD computation (χ^2 = 1.99, Fig. 2B, *left*). The fits from both XRD and MD-based models to the SAXS data were improved with NMA, yielding χ^2values equal to 1.12 and 1.16, respectively (Fig. 2A-B, *left* panels). Notably, when starting from XRD coordinates, the NMA-refined model displayed strong distortions not compatible with the basic configuration of the protein, as the dimerization helices were broken (Fig. 2A, *right*, red model). The final SAXS-validated MD model of SET/TAF-Iβ ΔC was therefore selected for further analysis (Fig. 2B, *right panel* and 2C, blue models; SASBDB entry SASDN77).

Additionally, we used SDSL-EPR and in particular, DEER experiments to evaluate the inter-label distance distribution between the two monomers of SET/TAF-Iβ ΔC and then evaluate its dynamics. For such purpose, five single-Cys mutants across SET/TAF-Iβ ΔC were designed, namely Q69C, S93C, S178C, A201C and D226C. Such Cys residues were utilized to graft MTSL nitroxide probes. By these means, we measured dipolar couplings between spin labels at the same position of each monomer. The chosen positions cover a convenient representation of locations and dynamics presumably experienced by the different SET/TAF-Iβ ΔC regions. It should be mentioned that these mutants were located at several stretches of the earmuffs, excepting for Gln69, which is located in the dimerization helix. DEER spectra analysis of the MTSL-labeled SET/TAF-Iβ ΔC mutants shown in Fig. S5 (black lines) clearly indicate broad and multimodal distance distributions for spin pairs placed on the earmuffs (all positions except 69), indicating a large distribution of orientations of one monomer with respect to the other. Interestingly, a bimodal distance distribution of spin labels (around 5 and 7 nm) were observed for position 69 (Fig. S5C), which is located at the dimerization helix; it suggests a movement of the earmuffs around the two dimeric helices, as depicted in Fig. S4B. This finding corroborates the abovementioned changes in the relative orientation of SET/TAF-Iβ ΔC observed in the MD simulations (Fig. S4B). Kratky plot obtained from SAXS measurements on the molecule further supported these observations, showing a marked flexible component together with a mainly globular profile

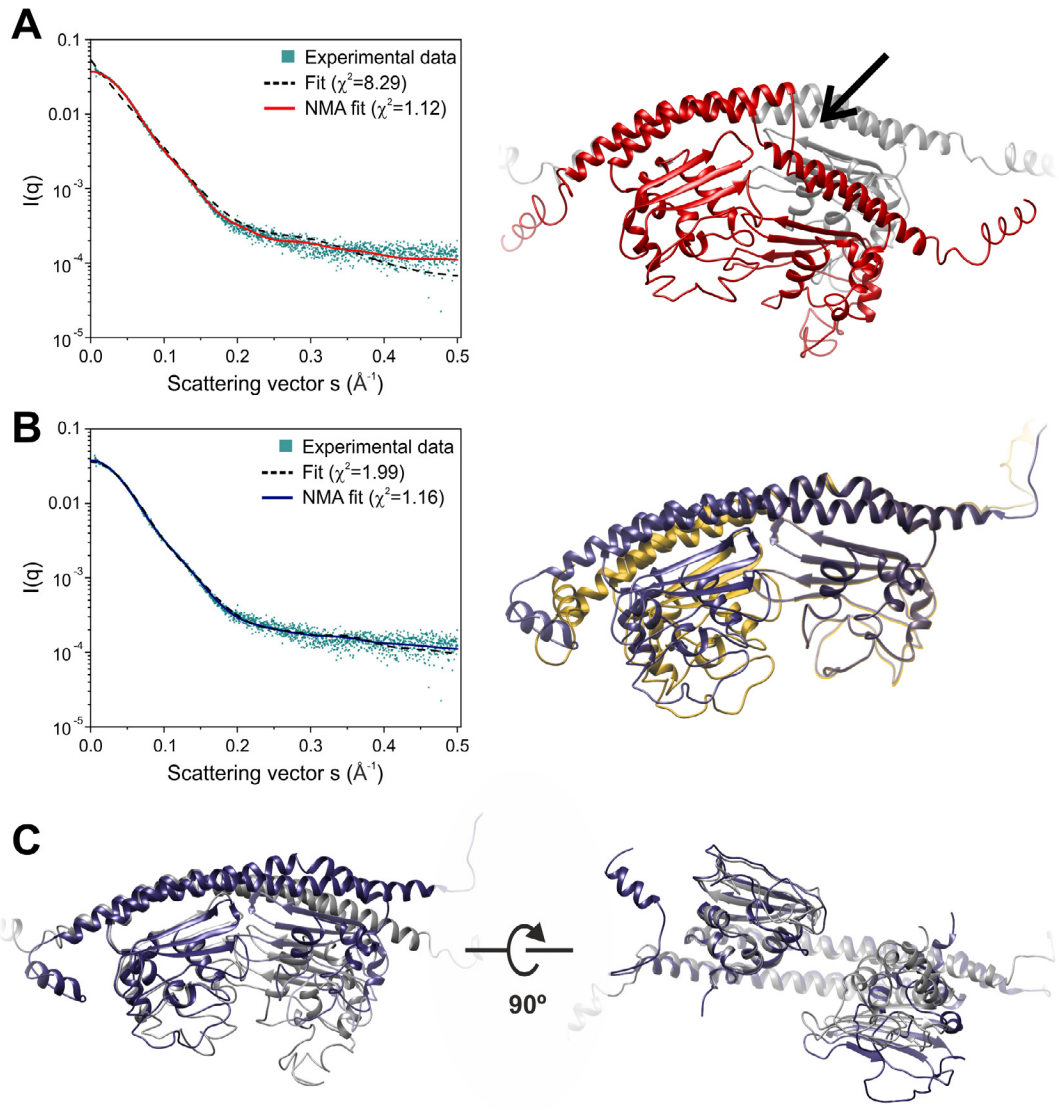

Fig. 2. SET/TAF-Iβ ΔC structural model provided by combining MD calculations with SAXS experimental approaches. (A) *Left* – Experimental scattering profile of SET/TAF-Iβ ΔC obtained by SAXS, fitting to the theoretical profile of SET/TAF-Iβ ΔC modified crystallographic structure (χ^2 = 8.29, dashed black line) and fitting after normal mode analysis (NMA) performed by SREFLEX (χ^2 = 1.12, solid red line). *Right* – Overlay of ribbon representations of the loop-refined crystallographic model of SET/TAF-Iβ ΔC (PDB entry 2E50 [16], grey) and the structure obtained after NMA refinement for SAXS fitting (red). Black arrow indicates a break of dimerization helices upon NMA refinement. Both models include flexible segments in earmuff domains built by MODELLER [66]. (B) *Left* – Experimental scattering profile of SET/TAF-Iβ ΔC obtained by SAXS are accompanied by the fits to the theoretical profile of the better MD structure before (χ^2 = 1.99, dashed black line) and after normal mode analysis NMA performed by SREFLEX (χ^2 = 1.16, solid blue line). *Right* – Overlay of ribbon representations of the structural model provided by MD that better fits SAXS experimental data (ocher) and the one obtained after NMA refinement (dark blue). (C) Overlay between the modified crystallographic model of SET/TAF-Iβ ΔC (grey) and the final SAXS-validated MD model (dark blue). (For interpretation of the references to colour in this figure legend, the reader is referred to the web version of this article.)

(Fig. S4C). The distances between each pair of spin-labeled residues calculated on the SAXS-validated MD model are included in the most populated states of distance distributions measured by DEER-EPR (Fig. S5). This data supports that the proposed SET/TAF-Iβ ΔC model (Fig. 2B, *right panel* and 2C) provides a very good representation of the average state of the molecule in solution.

In summary, both SAXS and DEER-EPR spectroscopic data, along with MD simulations, indicate that SET/TAF-Iβ ΔC possesses a highly flexible structure, despite having large ordered regions.

3.3. SET/TAF-Iβ ΔC earmuff domains are responsible for cytochrome c binding

To obtain structural information about the complex between SET/TAF-Iβ ΔC and C*c*, SAXS was utilized on a titration series with SET/TAF-Iβ ΔC:C*c* molar ratios of 1:0.5, 1:1, 1:2 and 1:4. Along the titration, R_g increased from 34 to 44 Å, the plateau being reached at a 1:2 molar ratio, suggesting that two molecules of C*c* bind to each SET/TAF-Iβ ΔC homodimer. In parallel, the maximum dimension (D_{max}) increased from 97 to 170 Å (Table S1). The data obtained at the highest titration ratio (1:4) were chosen for further analysis to ensure the full complex formation.

Fig. 3 shows the SAXS pattern obtained for the complex, from which a rigid body model was built using SASREF [81]. The best fit (χ^2 = 1.6) was found using the structure for SET/TAF-Iβ ΔC closest to average of the sampled trajectories by MD computations together with two C*c* molecules. These two hemeprotein molecules sample the SET/TAF-Iβ ΔC earmuffs, one of them being oriented towards the internal groove between the earmuffs and the other one placed at the external face of the other earmuff (Fig. 3; SASBDB entry SASDN87).

We further performed ITC measurements using SET/TAF-Iβ ΔC in complex with C*c* to study the thermodynamics of the interaction. At low ionic strength, the thermograms (Fig. S6) fitted to an independent binding sites model. Such fitting renders a stoichiometry value of 1.51 for the interaction (Table S2), which may be explained if the active protein fraction in the experiment is lower than the total amount. Thus, ITC experiments agree with SAXS measurements and SET/TAF-Iβ ΔC interacting with two C*c* molecules. Both binding events are thermodynamically equivalent, with affinities in the micromolar range (Table S2), as inferred from the monophasic profile of binding isotherms (Fig. S6A).

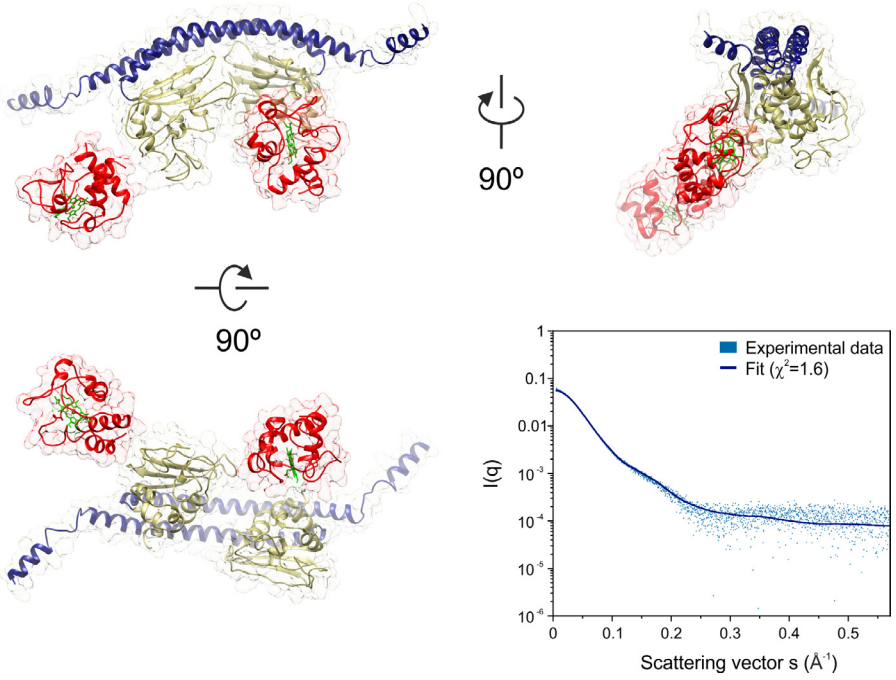

Fig. 3. SAXS data of SET/TAF-Iβ ΔC in complex with cytochrome *c*. SAXS model entails two molecules of C*c* sampling the globular domains of SET/TAF-Iβ ΔC. Ribbon and surface of SET/TAF-Iβ ΔC represent its dimerization domain in blue and earmuff domain in beige. Ribbon and transparent surface of C*c* is represented in red with the heme group in green. The fit (χ^2 = 1.6) of the experimental solution scattering profile to the theoretical profile (dark blue curve) is shown. (For interpretation of the references to colour in this figure legend, the reader is referred to the web version of this article.)

The analysis also showed that this interaction was endothermic and entropically-driven, suggesting that the driving forces leading to complex formation are mainly electrostatic and/or hydrophobic [82]. Hence, we assessed the abovementioned interaction at high ionic strength (Fig. S6B). The K_D value was substantially increased in the presence of 100 mM KCl when compared with the value obtained at low ionic strength (Table S2). This finding reveals a strongly electrostatic nature for the interaction, which is disrupted when the high net charges of both partners are shielded by counterions. A similar thermodynamic behavior was exhibited by the complex between C*c* and full-length SET/TAF-Iβ, with the binding affinity constant for the C*c*/SET/TAF-Iβ complex at moderate ionic strength (100 mM KCl) similar to that of C*c*/SET/TAF-Iβ ΔC at low salt (this manuscript). The biological relevance of the interaction between the histone chaperone and the hemeprotein was likewise corroborated in cell assays [47].

3.4. Cytochrome c explores the mobile globular domains of SET/TAF-Iβ ΔC in a highly dynamic and polyconformational manner

To better understand how C*c* explores the globular domains of SET/TAF-Iβ ΔC, we further analyzed the regions of the histone chaperone involved in the interaction, with particular emphasis on details about the protein intrinsic dynamics and flexibility. For such purpose, we performed CW-EPR and ^{19}F-NMR experiments making use of MTSL and BTFA probes grafted on different regions of SET/TAF-Iβ ΔC by profiting of the abovementioned designed mutants. Accordingly, either nitroxide MTSL spin probe or BTFA ^{19}F probes were covalently bound to Cys residues (Q69C, S93C, S178C, A201C and D226C; Fig. 4A and S7A).

CW X-band EPR spectra of each spin-labeled variant of SET/TAF-Iβ ΔC were recorded in the absence or in the presence of reduced C*c* in a 1:2 molar ratio (SET/TAF-Iβ ΔC:C*c*; Fig. 4B-D, *left* and Fig. S7B). EPR spectral shapes reflected different structural constraints exerted on the spin label by the surrounding structure (Fig. 4A and Fig. S7A). Noteworthy, the EPR spectra of Q69C^{MTSL} and S93C^{MTSL} species are broad (Fig. 4B-C, *left*), indicating that the spin label motions are restricted, in agreement with the label being in a well-structured environment. In addition, the S93C^{MTSL} spectrum displayed a broad and a narrow component, suggesting at least two exchanging conformations (Fig. 4C, *left*). Supporting this, MD computations (Fig. S4D) indicated that helix 4—which includes Ser93—is strained and exchanges between α, 3_{10} and turn conformations. On the contrary, S178C^{MTSL} and D226C^{MTSL} (Figs. S7, *left* and 4D, *left*) showed the highest mobility. Accordingly, these residues are not visible in the 3D X-ray structure, most likely due to the highly dynamic behavior of those regions.

The interaction of C*c* with the labeled SET/TAF-Iβ ΔC mutants hardly affected the dynamics of the grafted spin labels (Fig. 4B-D, *left* panels and Fig. S7B). The absence of significant alterations in spectral shapes indicates that the mobility of the spin labels (in the ns range) is not affected by the presence of C*c*. This suggests that C*c* might not occupy a specific position over a long time period but rather samples the multiple conformations of SET/TAF-Iβ in a transient manner. SPRi experiments on WT SET/TAF-Iβ ΔC or

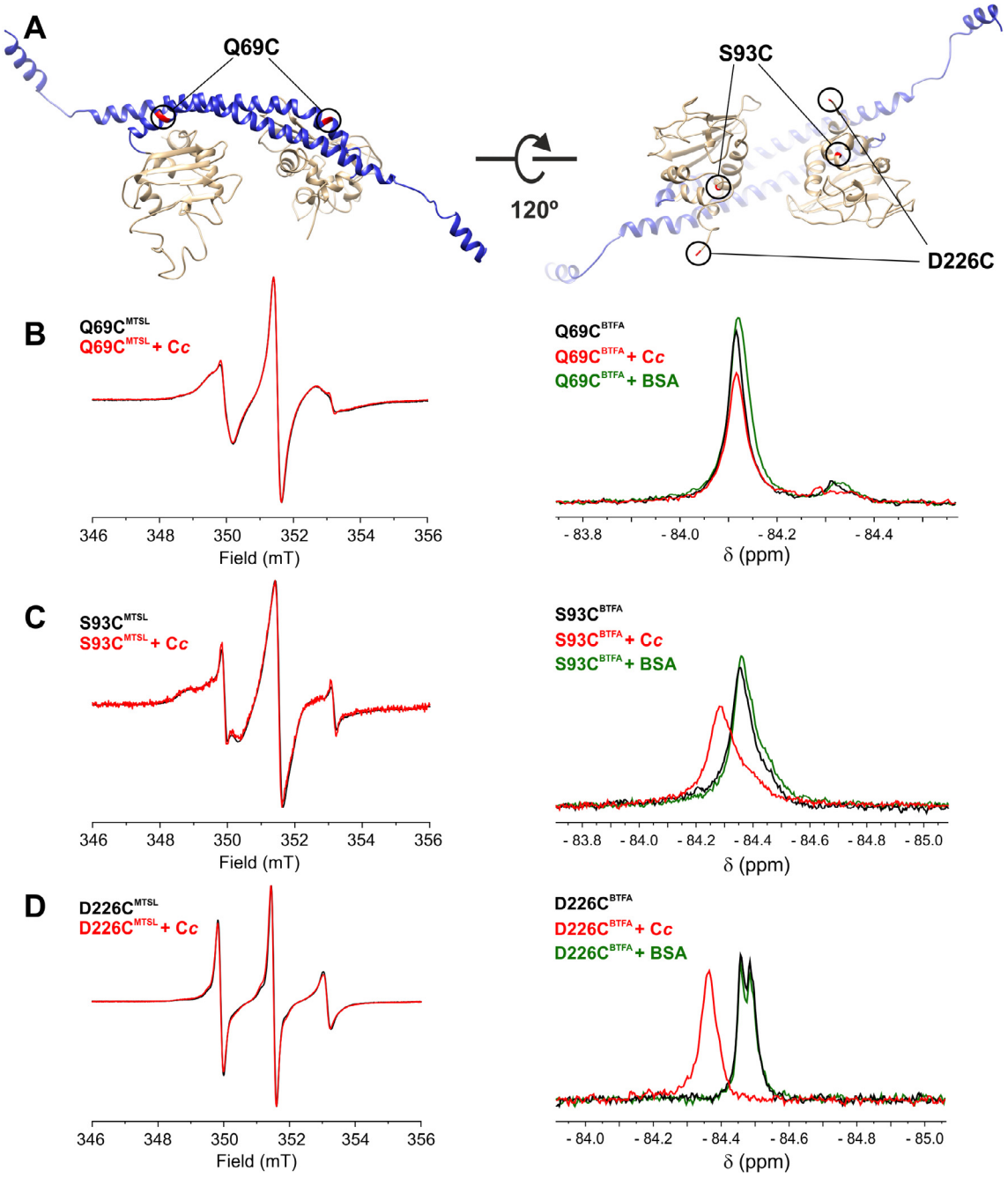

Fig. 4. Cytochrome *c* specifically targets SET/TAF-Iβ ΔC earmuff domains, as inferred from CW-EPR and ^{19}F-NMR. (A) Ribbon representation of SET/TAF-Iβ ΔC in two projections rotated 120° on the horizontal axis. Dimerization domains are represented in blue and earmuff domains in beige. Highlighted residues in red have been substituted by Cys (Q69C, S93C and D226C) to graft either MTSL nitroxide or BTFA ^{19}F probes. (B-D) Continuous-wave EPR (CW-EPR) spectra (*left* panels) and ^{19}F-NMR spectra (*right* panels) of MTSL and BTFA probes bound to Q69C (B), S93C (C) and D226C (D) SET/TAF-Iβ ΔC mutants. Spectra corresponding to free probe-bound SET/TAF-Iβ ΔC are in black, whereas those in complex with C*c* are in red. BSA (green) was used as a negative control in ^{19}F NMR. (For interpretation of the references to colour in this figure legend, the reader is referred to the web version of this article.)

D226C^{MTSL} allowed us to discard possible changes in affinity due to spin grafting at the interaction interface of SET/TAF-Iβ ΔC with C*c* (Fig. S8 and Table S3).

^{19}F-NMR spectra were acquired for the same Cys mutants labeled with the BTFA fluorine probe. Each BTFA-labeled SET/TAF-Iβ ΔC variant generated a signal at a specific chemical shift, indicating that they are exposed to different chemical environments and dynamics. We monitored chemical-shift and linewidth perturbations upon addition of C*c*, and upon addition of BSA as a negative control (Fig. 4B-D, *right* and Fig. S7C-D). S93C^{BTFA} and A201C^{BTFA} resonances underwent both line broadening and chemical-shift perturbation upon C*c* binding (Fig. 4C, *right* and Figs. S7C, *right*), thereby indicating that they are directly sampled by the hemeprotein. D226C^{BTFA} spectrum displayed two proximal resonances, which might correspond to two possible exchanging populations (Fig. 4D, *right*). The latter agrees with the high mobility of that region. Interestingly, such splitting disappears upon C*c* binding, alongside a chemical-shift perturbation (Fig. 4D, *right*). No changes in the ^{19}F signal upon addition of BSA were observed for any SET/TAF-Iβ ΔC variant (Fig. 4B-D, *left* and S7C, *right*). Note-

worthy, the S178C^{BTFA} signal showed a completely unspecific behavior, suffering C*c*-concentration independent chemical-shift perturbations and line broadening, even upon addition of BSA (Fig. S7C, *left*). With the aim of discarding a possible effect derived from the high conformational diversity of such region, we recorded the ^{19}F-NMR spectra at 7 °C (Fig. S7D). Interestingly, the ^{19}F signal was not affected by BSA under these conditions—in contrast with the spectrum recorded at 25 °C (Fig. S7C, *left*)—but broadened upon C*c* addition in a concentration-dependent manner. This behavior suggests that this region surrounding Ser178 is involved in C*c* recognition, even when sampling multiple conformational states.

In this context, we performed PRE-NMR measurements to map those residues at the C*c* surface that are affected upon binding to the different spin-labeled SET/TAF-Iβ ΔC variants. Fig. 5 shows the paramagnetic effects exerted by spin-labeled SET/TAF-Iβ ΔC mutants on C*c* amide signals, as well as their mappings on the C*c* surface. Almost no paramagnetic effect was observed on C*c* interacting with SET/TAF-Iβ ΔC Q69C^{MTSL} (Fig. 5A), in concordance with the ^{19}F-NMR data. On the contrary, when the spin probe was placed at Ser93 or Ala201 (Fig. 5B and S9A), we observed intense PRE effects circumscribed to the heme cleft region of C*c*, in agreement with our previous chemical-shift perturbation analysis [47,48]. A similar pattern along the C*c* surface was produced by the variant D226C^{MTSL} (Fig. 5C), but to a lesser extent. In this case, a more diffused pattern of C*c* affected residues can be explained by the moderate flexibility of the stretch containing Asp226. In a similar manner, spin label at Ser178 (Fig. S9B) produced a very faint and diffused pattern along the C*c* surface, accounting for the high flexibility and dynamics of the segments in which this residue is located. Thus, I_p/I_d values for S178C$^{MTS/MTSL}$ variants suggest a weaker sampling by C*c* of the bottom of earmuffs domains (position 178).

Altogether, these results hint the earmuffs of SET/TAF-Iβ as the effectors of the C*c* recognition rather than the dimerization helices. The NMR results point out that C*c* samples the surroundings of the SET/TAF-Iβ ΔC internal groove—partially involving the flexible loops at the bottom of the earmuffs—and exposing the surface nearby its heme group.

4. Discussion

In last years, the intrinsic flexibility of proteins has become increasingly important in the study of their intermolecular recognition mechanisms. Many protein complexes actually occur through an assorted ensemble of conformations, rather than fitting a classical model of static and well-defined binding sites. Within this frame, the occurrence of a multiconformational encountering interaction for the accomplishment of a biological function is especially enhanced when one of the partners exhibits high intrinsic dynamics [1]. This is the case with the multifunctional oncoprotein SET/TAF-Iβ, whose globular domains—earmuffs—are important in the recognition of its novel partner C*c*, as do they with histones [18,19] or PP2A [42]. Here, we show the role of the structured portion of SET/TAF-Iβ in C*c* binding, without ruling out the participation of the unstructured C-terminal acidic stretches in the binding of histones [19], PP2A [39,42] or also C*c* [47]. Our MD, SAXS and SDSL-EPR data show that SET/TAF-Iβ ΔC possesses a highly inherent flexibility of the two monomers within the dimer—in spite of its large ordered regions—which directly influences C*c* recognition. The structural characterization of this construct through MD and SAXS allowed us to analyze the dynamics of the flexible segments not visible in the crystallographic model (PDB 2E50 [18]), as well as the dynamic behavior of the entire structure. Such inherent flexibility of the structured region of SET/TAF-Iβ ΔC likely remains unaltered in the context of full-length SET/TAF-Iβ (Fig. S10A). Its unstructured acidic C-terminal tails are highly dynamic and establish a limited number of contacts with other regions of the protein (Fig. S10B). This contrasts with the case of the variant TAF-I α, whose helix 1 at the N-terminus is rich in basic residues (Arg and Lys) and is involved in multiple electrostatic intermolecular contacts with the acidic C-terminal tails, thus restraining their mobility and impairing the histone chaperone activity of the protein [83]. Additionally, DEER-EPR experiments have revealed the wide distribution of relative orientations experienced by the globular domains of SET/TAF-Iβ ΔC, pointing to their importance in the recognition of its partners, such as C*c*, through the modulation of the contact surface.

The nuclear interaction between C*c* and SET/TAF-Iβ has recently been described to regulate the histone chaperone activity of SET/TAF-Iβ under DNA damage conditions [47]. In this work, we report a new functional consequence of such interaction, i.e. the regulation of the PP2A inhibitory activity of SET/TAF-Iβ by C*c*. Such inhibition relies primarily in the structured portion of SET/TAF-Iβ, as evidenced by the ability of SET/TAF-Iβ ΔC to inhibit PP2A. Indeed, such a construct contains the regions which are mainly responsible for PP2A inhibition, comprising both the dimerization domain and the beginning of the earmuffs of SET/TAF-Iβ [42]. Thus, the competition between C*c* and PP2A for binding to the SET/TAF-Iβ earmuffs—or at least a part of them—might lead to abrogation of PP2A inhibition. In addition, alterations in the SET/TAF-Iβ ΔC intrinsic dynamics upon C*c* binding to the earmuffs—as demonstrated in this work—may induce drastic changes in the N-terminal region of SET/TAF-Iβ, also contributing to disrupt the recognition of PP2A by the chaperone. In fact, recent work from our group suggests that changes in the intrinsic dynamics can alter the binding process taking place in separated regions of such molecule [49].

The structural and dynamical analysis of the SET/TAF-Iβ ΔC:C*c* complex conducted in this work have allowed us to unveil the molecular mechanism subjacent to the C*c*-mediated blocking of the PP2A inhibition. SAXS and NMR analyses yielded a low-resolution model of the complex, displaying two C*c* binding sites, one at the inner groove between the earmuffs of the chaperone, and another one at the external face of these domains. Altogether, the data suggest that C*c* samples the earmuffs of SET/TAF-Iβ ΔC in a diffuse fashion and exploring multiple conformational states of the chaperone. It is widely accepted that SET/TAF-Iβ, along with other structural and functional analogues, use their internal groove to recognize histones [18,44–46]. However, all these chaperones harbor histones in a single, well-defined orientation, as inferred from solved structures (PDB entry 5G2E [84]). Such mode of interaction has a functional purpose, which is to keep histones soluble during chromatin remodeling. On the contrary, the diffuse nature of the SET/TAF-Iβ recognition by C*c* could agree with the regulatory role of the hemeprotein: i) blocking PP2A inhibition [this work], and ii) controlling (dis)assembly of chromatin [47]. Different interaction modes of SET/TAF-Iβ with its known partners—histones or C*c*—may represent a unique example in biology on how different functions require different molecular recognition mechanisms.

Herein, we decipher the molecular mechanism underlying the interaction in the nucleus of SET/TAF-Iβ with C*c* via the globular domains of the chaperone to form a polyconformational ensemble, thus providing insights about the newly discovered regulatory function of C*c*, i.e. regulation of an essential DDR phosphatase. This novel C*c* role, along with its ability to inhibit SET/TAF-Iβ histone chaperone activity and alter chromatin accessibility [47], further supports the relevance of extramitochondrial C*c* in the DDR regulation. In addition, we have recently reported the ability of C*c* to modulate PP2A activity by interacting with another PP2A inhibitor, namely ANP32B [49]. A potential role for C*c* regulating tumor progression by inducing PP2A release from its inhibitors SET/TAF-Iβ or

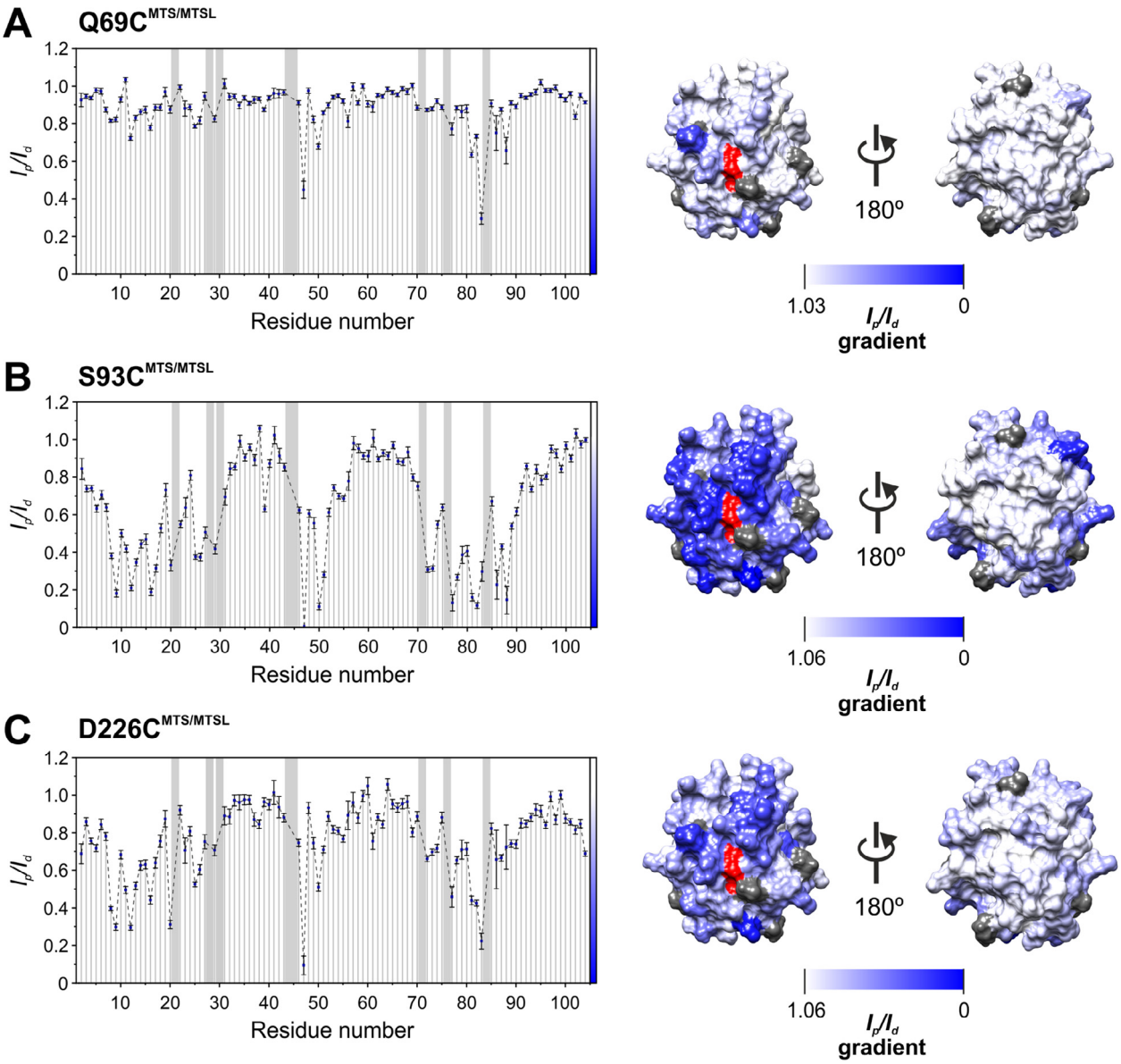

Fig. 5. Paramagnetic relaxation enhancement NMR effects of SET/TAF-Iβ ΔC binding on cytochrome *c* surface. For each SET/TAF-Iβ ΔC spin-labeled position–Q69C (A), S93C (B) and D226C (C)– the normalized I_p/I_d ratio (signal intensity in the paramagnetic sample by signal intensity in the diamagnetic sample) of C*c* residues is plotted in bar diagrams (*left* panels) and on the surface of the hemeprotein as a white to blue gradient (*right* panels; PDB entry 2N9I [80]). Heme group is colored in red. Prolines and non-assigned residues are represented with grey shadows or colored in grey at left and right panels, respectively. (For interpretation of the references to colour in this figure legend, the reader is referred to the web version of this article.)

ANP32B cannot be discarded, as disruption of PP2A inhibition by targeting SET/TAF-Iβ hinders the progression of certain kinds of tumors [38,85,86]. In this context, it is tempting to propose a plausible function for SET/TAF-Iβ and/or ANP32B in INTAC-mediated transcription, as well as a clear impact of nuclear C*c* over INTAC activity and its consequences in tumor development.

5. Conclusions

Taken together, our results herein presented shed light on the molecular mechanism of the polyconformational, diffuse ensemble between SET/TAF-Iβ oncoprotein and C*c*, and explain how the extramitochondrial hemeprotein regulates DDR by means of PP2A activation. Inducing PP2A release from its inhibitors, nuclear C*c* emerges as a cornerstone to understand the complex and intertwined PP2A regulatory network. Within this frame, mechanistic details of targeting SET/TAF-Iβ by C*c* may help in rational drug design to disrupt the progression of certain types of tumors.

CRediT authorship contribution statement

Miguel Á. Casado-Combreras: Conceptualization, Methodology, Software, Formal analysis, Investigation, Writing – original draft, Writing – review & editing, Visualization. **Francisco Rivero-Rodríguez:** Formal analysis, Investigation, Visualization. **Carlos A. Elena-Real:** Conceptualization, Methodology, Formal analysis, Investigation. **Dmitry Molodenskiy:** Formal analysis, Investigation. **Antonio Díaz-Quintana:** Software, Formal analysis. **Marlène Martinho:** Methodology, Formal analysis, Investigation, Writing – review & editing. **Guillaume Gerbaud:** Methodology, Formal analysis, Investigation. **Katiuska González-Arzola:** Writing – review & editing. **Adrián Velázquez-Campoy:** Formal analysis,

Writing – review & editing. **Dmitri Svergun:** Methodology, Formal analysis, Investigation, Resources, Writing – review & editing. **Valérie Belle:** Methodology, Formal analysis, Investigation, Resources, Writing – review & editing. **Miguel A. De la Rosa:** Conceptualization, Supervision, Writing – review & editing, Funding acquisition. **Irene Díaz-Moreno:** Conceptualization, Supervision, Investigation, Writing – review & editing, Project administration, Funding acquisition.

Declaration of Competing Interest

The authors declare that they have no known competing financial interests or personal relationships that could have appeared to influence the work reported in this paper.

Acknowledgements

This work was supported by Ministry of Science and Innovation (PID2021-126663NB-I00, PGC2018-096049-B-I00 and BFU2015-71017), European Regional Development Fund (FEDER), Andalusian Government (BIO-198, US-1254317, US-1257019, P18-FR-3487 and P18-HO-4091), University of Seville (VI PPIT) and the Ramón Areces Foundation. This work was also supported by Ministry of Education and Professional Training (FPU18/06577 and FPU013/04373 for M. A. C. C. and F. R. R., respectively), Biointeractomics Platform (cicCartuja, Seville) and the NMR Services at CITIUS (University of Seville). D. M. and D. S. acknowledge the support by the German Federal Ministry of Education and Research, project FKZ 16QK10A. For EPR studies, financial support from the IR INFRANALYTICS FR2054 for conducting the research is gratefully acknowledged. Authors also thank the COST MOBIEU (CA15126) for support in Short Term Scientific Missions. Molecular graphics and analyses performed with UCSF Chimera, developed by the Resource for Biocomputing, Visualization, and Informatics at the University of California, San Francisco, with support from NIH P41-GM103311. Authors thank Prof. M. Horikoshi for the kind gift of the plasmid encoding SET/TAF-Iβ ΔC. Authors also acknowledge Mr. Abraham Muñiz-Chicharro for his invaluable support with computational work.

Appendix A. Supplementary data

Supplementary data to this article can be found online at https://doi.org/10.1016/j.csbj.2022.07.009.

References

[1] Dunker AK, Silman I, Uversky VN, Sussman JL. Function and structure of inherently disordered proteins. Curr Opin Struct Biol 2008;18:756–64.
[2] Levitt M. Nature of the protein universe. Proc Natl Acad Sci USA 2009;106:11079–84.
[3] Chakravarty D, Janin J, Robert CH, Chakrabarti P. Changes in protein structure at the interface accompanying complex formation. Int Union Crystallogr J 2015;2:643–52.
[4] Kozakov D, Li K, Hall DR, et al. Encounter complexes and dimensionality reduction in protein-protein association. eLife 2014;3:e01370.
[5] Ubbink M. The courtship of proteins: understanding the encounter complex. FEBS Lett 2009;583:1060–6.
[6] Tompa P, Fuxreiter M. Fuzzy complexes: polymorphism and structural disorder in protein-protein interactions. Trends Biochem Sci 2008;33:2–8.
[7] Vinogradova O, Qin J. NMR as a unique tool in assessment and complex determination of weak protein-protein interactions. Top Curr Chem 2012;326:35–45.
[8] Shrestha UR, Juneja P, Zhang Q, et al. Generation of the configurational ensemble of an intrinsically disordered protein from unbiased molecular dynamics simulation. Proc Natl Acad Sci USA 2019;116:20446–52.
[9] Kikhney AG, Svergun DI. A practical guide to small angle X-ray scattering (SAXS) of flexible and intrinsically disordered proteins. FEBS Lett 2015;589:2570–7.
[10] Liu Z, Gong Z, Dong X, Tang C. Transient protein-protein interactions visualized by solution NMR. Biochim Biophys Acta 2016;1864:115–22.
[11] Iwahara J, Clore GM. Detecting transient intermediates in macromolecular binding by paramagnetic NMR. Nature 2006;440:1227–30.
[12] Sára T, Schwarz TC, Kurzbach D, et al. Magnetic resonance access to transiently formed protein complexes. ChemistryOpen 2014;3:115–23.
[13] Bashir Q, Volkov AN, Ullmann GM, Ubbink M. Visualization of the encounter ensemble of the transient electron transfer complex of cytochrome *c* and cytochrome *c* peroxidase. J Am Chem Soc 2010;132:241–7.
[14] Kim YC, Tang C, Clore GM, Hummer G. Replica exchange simulations of transient encounter complexes in protein-protein association. Proc Natl Acad Sci USA 2008;2:12855–60.
[15] Tang C, Iwahara J, Clore GM. Visualization of transient encounter complexes in protein-protein association. Nature 2006;444:383–6.
[16] Le Breton N, Martinho M, Mileo E, et al. Exploring intrinsically disordered protein using site-directed spin labeling electron paramagnetic resonance spectroscopy. Front Mol BioSci 2015;2:21.
[17] Torricella F, Pierro A, Mileo E, Belle V, Bonucci A. Nitroxide spin labels and EPR spectroscopy: a powerful association for protein dynamics studies. Biochim Biophys Acta – Proteins Proteom 2021;1869:140653.
[18] Muto S, Senda M, Akai Y, et al. Relationship between the structure of SET/TAF-Iβ/INHAT and its histone chaperone activity. Proc Natl Acad Sci USA 2007;104:4285–90.
[19] Karetsou Z, Emmanouilidou A, Sanidas I, et al. Identification of distinct SET/TAF-Iβ domains required for core histone binding and quantitative characterisation of the interaction. BMC Biochem 2009;10:10.
[20] Kalousi A, Hoffbeck AS, Selemenakis PN, et al. The nuclear oncogene SET controls DNA repair by KAP1 and HP1 retention to chromatin. Cell Rep 2015;11:149–63.
[21] Mandemaker IK, Zhou D, Bruens ST, et al. Histone H1 eviction by the histone chaperone SET reduces cell survival following DNA damage. J Cell Sci 2020;133:jcs235473.
[22] Cho I, Tsai P-F, Lake RJ, Basheer A, Fan H-Y. ATP-dependent chromatin remodeling by Cockayne Syndrome Protein B and NAP1-like histone chaperones is required for efficient transcription-coupled DNA repair. PLoS Genet 2013;9:e1003407.
[23] Adam S, Polo SE. Blurring the line between the DNA damage response and transcription: the importance of chromatin dynamics. Exp Cell Res 2014;329:148–53.
[24] Li M, Guo H, Damuni Z. Purification and characterization of two potent heat-stable protein inhibitors of protein phosphatase 2A from bovine kidney. Biochemistry 1995;34:1988–96.
[25] Li M, Makkinje A, Damuni Z. The myeloid leukemia-associated protein SET is a potent inhibitor of protein phosphatase 2A. J Biol Chem 1996;271:11059–62.
[26] Ramos F, Villoria MT, Alonso-Rodríguez E, Clemente-Blanco A. Role of protein phosphatases PP1, PP2A, PP4 and Cdc14 in the DNA damage response. Cell Stress 2019;3:70–85.
[27] Chowdhury D, Keogh M-C, Ishii H, et al. γ -H2AX dephosphorylation by protein phosphatase 2A facilitates DNA double-strand break repair. Mol Cell 2005;20:801–9.
[28] Feng J, Wakeman T, Yong S, et al. Protein phosphatase 2A-dependent dephosphorylation of replication protein A is required for the repair of DNA breaks induced by replication stress. Mol Cell Biol 2009;29:5696–709.
[29] Zheng H, Qi Y, Hu S, et al. Identification of Integrator-PP2A complex (INTAC), an RNA polymerase II phosphatase. Science 2020;370:eabb5872.
[30] Huang KL, Jee D, Stein CB, et al. Integrator recruits protein phosphatase 2A to prevent pause release and facilitate transcription termination. Mol Cell 2020;80:345–58.
[31] Fianu I, Chen Y, Dienemann C, et al. Structural basis of Integrator-mediated transcription regulation. Science 2021;374:883–7.
[32] Eichhorn PJ, Creyghton MP, Bernards R. Protein phosphatase 2A regulatory subunits and cancer. Biochim Biophys Acta 2009;1795:1–15.
[33] Curtis C, Shah SP, Chin S-F, et al. The genomic and transcriptomic architecture of 2,000 breast tumours reveals novel subgroups. Nature 2012;486:346–52.
[34] Pandey P, Seshacharyulu P, Das S, et al. Impaired expression of protein phosphatase 2A subunits enhances metastatic potential of human prostate cancer cells through activation of AKT pathway. Br J Cancer 2013;108:2590–600.
[35] Calin GA, di Iasio MG, Caprini E, et al. Low frequency of alterations of the α (PPP2R1A) and β (PPP2R1B) isoforms of the subunit A of the serine-threonine phosphatase 2A in human neoplasms. Oncogene 2000;19:1191–5.
[36] Vervoort SJ, Welsh SA, Devlin JR, et al. The PP2A-Integrator-CDK9 axis fine-tunes transcription and can be targeted therapeutically in cancer. Cell 2021;184:3143–3162.e32.
[37] Janghorban M, Farrell AS, Allen-Petersen BL, et al. Targeting c-MYC by antagonizing PP2A inhibitors in breast cancer. Proc Natl Acad Sci USA 2014;111:9157–62.
[38] Liu C-Y, Huang T-T, Chen Y-T, et al. Targeting SET to restore PP2A activity disrupts an oncogenic CIP2A-feedforward loop and impairs triple negative breast cancer progression. EBioMedicine 2019;40:263–75.
[39] Arnaud L, Chen S, Liu F, et al. Mechanism of inhibition of PP2A activity and abnormal hyperphosphorylation of tau by I_2^{PP2A}/SET. FEBS Lett 2011;585:2653–9.
[40] Switzer C, Cheng R, Vitek T, et al. Targeting SET/I_2PP2A oncoprotein functions as a multi-pathway strategy for cancer therapy. Oncogene 2011;30:2504–13.
[41] Arif M, Wei J, Zhang Q, et al. Cytoplasmic retention of protein phosphatase 2A inhibitor 2 (I_2^{PP2A}) induces Alzheimer-like abnormal hyperphosphorylation of Tau. J Biol Chem 2014;289:27677–91.

[42] Saito S, Miyaji-Yamaguchi M, Shimoyama T, Nagata K. Functional domains of Template-Activating Factor-I as a protein phosphatase 2A inhibitor. Biochem Biophys Res Commun 1999;259:471–5.
[43] De Palma RM, Parnham SR, Li Y, et al. The NMR-based characterization of the FTY720-SET complex reveals an alternative mechanism for the attenuation of the inhibitory SET-PP2A interaction. FASEB J. 2019;33. fj.201802264R.
[44] Park YJ, Luger K. The structure of nucleosome assembly protein 1. Proc Natl Acad Sci USA 2006;103:1248–53.
[45] Tang Y, Meeth K, Jiang E, Luo C, Marmorstein R. Structure of Vps75 and implications for histone chaperone function. Proc Natl Acad Sci USA 2008;105:12206–11.
[46] Gill J, Yogavel M, Kumar A, et al. Crystal structure of malaria parasite nucleosome assembly protein: distinct modes of protein localization and histone recognition. J Biol Chem 2009;284:10076–87.
[47] González-Arzola K, Díaz-Moreno I, Cano-González A, et al. Structural basis for inhibition of the histone chaperone activity of SET/TAF-Iβ by cytochrome *c*. Proc Natl Acad Sci USA 2015;112:9908–13.
[48] Martínez-Fábregas J, Díaz-Moreno I, González-Arzola K, et al. Structural and functional analysis of novel human cytochrome *c* targets in apoptosis. Mol Cell Proteomics 2014;13:1439–56.
[49] Rivero-Rodríguez F, Díaz-Quintana A, Velázquez-Cruz A, et al. Inhibition of the PP2A activity by the histone chaperone ANP32B is long-range allosterically regulated by respiratory cytochrome *c*. Redox Biol 2021;43:101967.
[50] Nagata K, Kawase H, Handa H, et al. Replication factor encoded by a putative oncogene, set, associated with myeloid leukemogenesis. Proc Natl Acad Sci USA 1995;92:4279–83.
[51] Olteanu A, Patel CN, Dedmon MM, et al. Stability and apoptotic activity of recombinant human cytochrome *c*. Biochem Biophys Res Commun 2003;312:733–40.
[52] Moreno-Beltrán B, Díaz-Moreno I, González-Arzola K, et al. Respiratory complexes III and IV can each bind two molecules of cytochrome *c* at low ionic strength. FEBS Lett 2015;589:476–83.
[53] Kingston RE, Chen CA, Rose JK. Calcium phosphate transfection. In: Ausubel Frederick M, editor. Curr Protoc in Mol Biol. John Wiley and Sons Inc: Hoboken, NJ, USA; 2003. p. 1–11. Chapter 9.
[54] Bradford MM. A rapid and sensitive method for the quantitation of microgram quantities of protein utilizing the principle of protein-dye binding. Anal Biochem 1976;72:248–54.
[55] Kelly S, Price N. The use of circular dichroism in the investigation of protein structure and function. Curr Protein Pept Sci 2005;1:349–84.
[56] Blanchet CE, Spilotros A, Schwemmer F, et al. Versatile sample environments and automation for biological solution X-ray scattering experiments at the P12 beamline (PETRA III, DESY). J Appl Crystallogr 2015;48:431–43.
[57] Graewert MA, Franke D, Jeffries CM, et al. Automated pipeline for purification, biophysical and X-ray analysis of biomacromolecular solutions. Sci Rep 2015;5:1–8.
[58] Round A, Felisaz F, Fodinger L, et al. BioSAXS Sample Changer: a robotic sample changer for rapid and reliable high-throughput X-ray solution scattering experiments. Acta Crystallogr Sect D Biol Crystallogr 2015;71:67–75.
[59] Franke D, Kikhney AG, Svergun DI. Automated acquisition and analysis of small angle X-ray scattering data. Nucl Instrum Methods Phys Res A 2012;689:52–9.
[60] Konarev PV, Volkov VV, Sokolova AV, Koch MHJ, Svergun DI. PRIMUS: a Windows PC-based system for small-angle scattering data analysis. J Appl Crystallogr 2003;36:1277–82.
[61] Mylonas E, Hascher A, Bernadó P, et al. Domain conformation of tau protein studied by solution small-angle X-ray scattering. Biochemistry 2008;47:10345–53.
[62] Hajizadeh NR, Franke D, Jeffries CM, Svergun DI. Consensus Bayesian assessment of protein molecular mass from solution X-ray scattering data. Sci Rep 2018;8:7204.
[63] Svergun D, Barberato C, Koch M. CRYSOL - A program to evaluate X-ray solution scattering of biological macromolecules from atomic coordinates. J Appl Crystallogr 1995;28:768–73.
[64] Panjkovich A, Svergun DI. Deciphering conformational transitions of proteins by small angle X-ray scattering and normal mode analysis. Phys Chem Phys 2016;18:5707–19.
[65] Petoukhov MV, Svergun DI. Applications of small-angle X-ray scattering to biomacromolecular solutions. Int J Biochem Cell Biol 2013;45:429–37.
[66] Case D, Betz R, Cerutti D, et al. AMBER 2016. San Francisco: University of California; 2016.
[67] Maier JA, Martinez C, Kasavajhala K, et al. ff14SB: improving the accuracy of protein side chain and backbone parameters from ff99SB. J Chem Theory Comput 2015;11:3696–713.
[68] Webb B, Sali A. Protein structure modeling with MODELLER. Methods Mol Biol 2017;1654:39–54.
[69] Izadi S, Anandakrishnan R, Onufriev AV. Building water models: a different approach. J Phys Chem Lett 2014;5:3863–71.
[70] Andersen HC. Molecular dynamics simulations at constant pressure and/or temperature. J Chem Phys 1980;72:2384.
[71] Ryckaert JP, Ciccotti G, Berendsen HJ. Numerical integration of the cartesian equations of motion of a system with constraints: molecular dynamics of n-alkanes. J Comput Phys 1977;23:327–41.
[72] Hamelberg D, Mongan J, McCammon JA. Accelerated molecular dynamics: a promising and efficient simulation method for biomolecules. J Chem Phys 2004;120:11919–29.
[73] Eastman P, Swails J, Chodera JD, et al. OpenMM 7: Rapid development of high performance algorithms for molecular dynamics. PLoS Comput Biol 2017;13:e1005659.
[74] Roe DR, Cheatham TE. PTRAJ and CPPTRAJ: software for processing and analysis of molecular dynamics trajectory data. J Chem Theory Comput 2013;9:3084–95.
[75] Franke D, Petoukhov M, Konarev P, et al. ATSAS 2.8: a comprehensive data analysis suite for small-angle scattering from macromolecular solutions. J Appl Crystallogr 2017;50:1212–25.
[76] McGibbon RT, Beauchamp KA, Harrigan MP, et al. MDTraj: a modern open library for the analysis of molecular dynamics trajectories. Biophys J 2015;109:1528–32.
[77] Pettersen EF, Goddard TD, Huang CC, et al. UCSF Chimera - a visualization system for exploratory research and analysis. J Comput Chem 2004;25:1605–12.
[78] Jeschke G, Chechik V, Ionita P, et al. DeerAnalysis2006 - a comprehensive software package for analyzing pulsed ELDOR data. Appl Magn Reson 2006;30:473–98.
[79] Lee W, Tonelli M, Markley JL. NMRFAM-SPARKY: enhanced software for biomolecular NMR spectroscopy. Bioinformatics 2015;31:1325–7.
[80] Imai M, Saio T, Kumeta H, et al. Investigation of the redox-dependent modulation of structure and dynamics in human cytochrome *c*. Biochem Biophys Res Commun 2016;469:978–84.
[81] Petoukhov MV, Svergun DI. Global rigid body modeling of macromolecular complexes against small-angle scattering data. Biophys J 2005;89:1237–50.
[82] Cooper A. Heat capacity effects in protein folding and ligand binding: a re-evaluation of the role of water in biomolecular thermodynamics. Biophys Chem 2005;115:89–97.
[83] Kajitani K, Kato K, Nagata K. Histone H1 chaperone activity of TAF-I is regulated by its subtype-dependent intramolecular interaction. Genes Cells 2017;22:334–47.
[84] Aguilar-Gurrieri C, Larabi A, Vinayachandran V, et al. Structural evidence for Nap1-dependent H2A–H2B deposition and nucleosome assembly. EMBO J 2016;35:1465–82.
[85] Serifi I, Besta S, Karetsou Z, et al. Targeting of SET/I_2PP2A oncoprotein inhibits Gli1 transcription revealing a new modulator of Hedgehog signaling. Sci Rep 2021;11:13940.
[86] Goswami S, Mani R, Nunes J, et al. PP2A is a therapeutically targetable driver of cell fate decisions via a c-Mys/p21 axis in Acute Myeloid Leukemia. Blood 2021. blood.2020010344.